Study of nonstandard neutrino interactions with atmospheric neutrino data in Super-Kamiokande I and II

G. Mitsuka,[2,*] K. Abe,[1] Y. Hayato,[1,3] T. Iida,[1] M. Ikeda,[1] J. Kameda,[1] Y. Koshio,[1] M. Miura,[1] S. Moriyama,[1,3] M. Nakahata,[1,3] S. Nakayama,[1] Y. Obayashi,[1] H. Sekiya,[1] M. Shiozawa,[1,3] Y. Suzuki,[1,3] A. Takeda,[1] Y. Takenaga,[1] Y. Takeuchi,[1,3] K. Ueno,[1] K. Ueshima,[1] H. Watanabe,[1] S. Yamada,[1] S. Hazama,[2] I. Higuchi,[2] C. Ishihara,[2] H. Kaji,[2] T. Kajita,[2,3] K. Kaneyuki,[2,3,†] H. Nishino,[2] K. Okumura,[2] N. Tanimoto,[2] F. Dufour,[4] E. Kearns,[4,3] M. Litos,[4] J. L. Raaf,[4] J. L. Stone,[4,3] L. R. Sulak,[4] M. Goldhaber,[5,†] K. Bays,[6] J. P. Cravens,[6] W. R. Kropp,[6] S. Mine,[6] C. Regis,[6] M. B. Smy,[6,3] H. W. Sobel,[6,3] M. R. Vagins,[6,3] K. S. Ganezer,[7] J. Hill,[7] W. E. Keig,[7] J. S. Jang,[8] J. Y. Kim,[8] I. T. Lim,[8] J. Albert,[9] K. Scholberg,[9,3] C. W. Walter,[9,3] R. Wendell,[9] T. Ishizuka,[10] S. Tasaka,[11] J. G. Learned,[12] S. Matsuno,[12] Y. Watanabe,[13] T. Hasegawa,[14] T. Ishida,[14] T. Ishii,[14] T. Kobayashi,[14] T. Nakadaira,[14] K. Nakamura,[14,3] K. Nishikawa,[14] Y. Oyama,[14] K. Sakashita,[14] T. Sekiguchi,[14] T. Tsukamoto,[14] A. T. Suzuki,[15] A. Minamino,[16] T. Nakaya,[16,3] M. Yokoyama,[16] Y. Fukuda,[17] Y. Itow,[18] T. Tanaka,[18] C. K. Jung,[19] G. Lopez,[19] C. McGrew,[19] C. Yanagisawa,[19] N. Tamura,[20] Y. Idehara,[21] M. Sakuda,[21] Y. Kuno,[22] M. Yoshida,[22] S. B. Kim,[23] B. S. Yang,[23] H. Okazawa,[24] Y. Choi,[25] H. K. Seo,[25] Y. Furuse,[26] K. Nishijima,[26] Y. Yokosawa,[26] M. Koshiba,[27] Y. Totsuka,[27,†] S. Chen,[28] J. Liu,[28] Y. Heng,[28] Z. Yang,[28] H. Zhang,[28] D. Kielczewska,[29] K. Connolly,[30] E. Thrane,[30] and R. J. Wilkes[30]

(The Super-Kamiokande Collaboration)

[1]*Kamioka Observatory, Institute for Cosmic Ray Research, University of Tokyo, Kamioka, Gifu 506-1205, Japan*
[2]*Research Center for Cosmic Neutrinos, Institute for Cosmic Ray Research, University of Tokyo, Kashiwa, Chiba 277-8582, Japan*
[3]*Institute for the Physics and Mathematics of the Universe, University of Tokyo, Kashiwa, Chiba 277-8582, Japan*
[4]*Department of Physics, Boston University, Boston, Massachusetts 02215, USA*
[5]*Physics Department, Brookhaven National Laboratory, Upton, New York 11973, USA*
[6]*Departmentyes of Physics and Astronomy, University of California, Irvine, Irvine, California 92697-4575, USA*
[7]*Department of Physics, California State University, Dominguez Hills, Carson, California 90747, USA*
[8]*Department of Physics, Chonnam National University, Kwangju 500-757, Korea*
[9]*Department of Physics, Duke University, Durham, North Carolina 27708, USA*
[10]*Junior College, Fukuoka Institute of Technology, Fukuoka, Fukuoka 811-0295, Japan*
[11]*Department of Physics, Gifu University, Gifu, Gifu 501-1193, Japan*
[12]*Department of Physics and Astronomy, University of Hawaii, Honolulu, Hawaii 96822, USA*
[13]*Physics Division, Department of Engineering, Kanagawa University, Kanagawa, Yokohama 221-8686, Japan*
[14]*High Energy Accelerator Research Organization (KEK), Tsukuba, Ibaraki 305-0801, Japan*
[15]*Department of Physics, Kobe University, Kobe, Hyogo 657-8501, Japan*
[16]*Department of Physics, Kyoto University, Kyoto, Kyoto 606-8502, Japan*
[17]*Department of Physics, Miyagi University of Education, Sendai, Miyagi 980-0845, Japan*
[18]*Solar Terrestrial Environment Laboratory, Nagoya University, Nagoya, Aichi 464-8602, Japan*
[19]*Department of Physics and Astronomy, State University of New York, Stony Brook, New York 11794-3800, USA*
[20]*Department of Physics, Niigata University, Niigata, Niigata 950-2181, Japan*
[21]*Department of Physics, Okayama University, Okayama, Okayama 700-8530, Japan*
[22]*Department of Physics, Osaka University, Toyonaka, Osaka 560-0043, Japan*
[23]*Department of Physics, Seoul National University, Seoul 151-742, Korea*
[24]*Department of Informatics in Social Welfare, Shizuoka University of Welfare, Yaizu, Shizuoka, 425-8611, Japan*
[25]*Department of Physics, Sungkyunkwan University, Suwon 440-746, Korea*
[26]*Department of Physics, Tokai University, Hiratsuka, Kanagawa 259-1292, Japan*
[27]*The University of Tokyo, Bunkyo, Tokyo 113-0033, Japan*
[28]*Department of Engineering Physics, Tsinghua University, Beijing, 100084, China*
[29]*Institute of Experimental Physics, Warsaw University, 00-681 Warsaw, Poland*
[30]*Department of Physics, University of Washington, Seattle, Washington 98195-1560, USA*
(Received 9 September 2011; published 14 December 2011)

In this paper we study nonstandard neutrino interactions as an example of physics beyond the standard model using atmospheric neutrino data collected during the Super-Kamiokande I (1996–2001) and II (2003–2005) periods. We focus on flavor-changing-neutral-currents (FCNC), which allow neutrino flavor

[*]Present address: Solar Terrestrial Environment Laboratory, Nagoya University, Nagoya, Aichi 464-8602, Japan
[†]Deceased.

transitions via neutral current interactions, and effects which violate lepton nonuniversality and give rise to different neutral-current interaction-amplitudes for different neutrino flavors. We obtain a limit on the FCNC coupling parameter, $\varepsilon_{\mu\tau}$, $|\varepsilon_{\mu\tau}| < 1.1 \times 10^{-2}$ at 90% C.L. and various constraints on other FCNC parameters as a function of the nonuniversality coupling, ε_{ee}. We find no evidence of nonstandard neutrino interactions in the Super-Kamiokande atmospheric data.

DOI: 10.1103/PhysRevD.84.113008 PACS numbers: 13.15.+g, 14.60.Pq, 14.60.St

I. INTRODUCTION

The experimental understanding of neutrino oscillations has improved dramatically over the last ten years. In 1998 Super-Kamiokande (''Super-K'') reported an up-down asymmetry in the zenith angle distribution of muonlike (μ-like) events and concluded the distortion was evidence for neutrino oscillations [1]. Super-K also observed an oscillation signature consistent with the L/E (path-length over energy) dependence predicted by ν_μ to ν_τ oscillations at maximal θ_{23} mixing [2]. Results consistent with the $\nu_\mu \rightarrow \nu_\tau$ oscillation hypothesis have also been obtained by the tau appearance analysis in Super-K [3] and the long-baseline accelerator experiments K2K [4] and MINOS [5].

However, many alternatives to neutrino oscillations have been proposed to explain the asymmetry of the atmospheric neutrino μ-like event sample [6]. Neutrino decoherence [7,8], neutrino decay [9,10], mass-varying neutrinos [11], and CPT violation effects are among the most prominent. Although most of these approaches have been ruled out by the Super-K [2,12] and MINOS [5] data, nonstandard neutrino interactions (NSI) with matter, that is interactions which are not predicted by the standard model, remain viable.

Among the many types of NSI models, we focus in this paper on two generic types of neutrino interactions. Flavor-changing-neutral-current (FCNC) effects represent neutrino interactions with fermions, f, in matter that induce neutrino flavor change: $\nu_\alpha + f \rightarrow \nu_\beta + f$, where α and β denote neutrino flavors. Lepton nonuniversal (NU) interactions, on the other hand, are defined by a nonuniversal neutral current scattering amplitude among the three flavored neutrinos. In the standard model, this amplitude is identical among the neutrinos. Other theories of neutrino mass, however, predict these kinds of interactions. For instance, NSI interactions are often seen in models where an effective off-diagonal neutral current appears in a phenomenological interaction [13], in models where neutrino mixing arises from admixtures of neutral heavy leptons [14,15], and in models with R-parity violating supersymmetry [16].

A summary of various NSI models is presented in Ref. [17]. Although NSI are predicted by various theories, the expected phenomena do not generally depend on the particular phenomenological model and are typically characterized by dependence on the neutrino energy and the surrounding matter density. For this reason, NSI can be explored in a general context using atmospheric neutrinos. While the current constraints on NSI come from beam-based experiments [18,19], atmospheric neutrinos can provide additional sensitivity to these interactions due to their ample flux and the large amount of matter they traverse before detection.

This paper discusses atmospheric neutrino oscillations in the context of NSI at Super-K and is organized as follows. The data set and oscillation framework used in this paper are presented in Secs. II and III, respectively. In Sec. IV we show the results of an analysis assuming two-flavor $\nu_\mu \leftrightarrow \nu_\tau$ neutrino oscillations amidst NSI. An analysis using an extended three-flavor framework is performed in Sec. V and finally, the results are summarized in Sec. VII.

II. ATMOSPHERIC NEUTRINO DATA

Super-K is a 50 kt water Cerenkov detector located in a zinc mine in Kamioka, Japan. It is optically separated into an inner detector (ID) which is instrumented with 11 146 inward facing photomultiplier tubes (PMTs) at full capacity, and an outer detector (OD) used to veto cosmic-ray muons. A more detailed description of the detector is presented in Ref. [20]. The run period of Super-K has been classified into four phases: The first phase corresponds to physics data taken between April 1996 and July 2001 (SK-I). After an accident at the end of 2001, Super-K resumed data taking with half the number of ID PMTs between October 2002 and October 2005 (SK-II). The remaining two run periods are divided into SK-III (2006–2008), after rebuilding the ID with its full complement of PMTs, and SK-IV (2008–present), after the data acquisition system was upgraded. In this paper we use data from the SK-I and SK-II run periods.

A. Classification Of atmospheric neutrino data

Atmospheric neutrino events in Super-K are divided into the following four categories: fully contained (FC), partially contained (PC), upward stopping muons (UPMU stopping) and upward through-going muons (UPMU through-going). For FC and PC events, event vertices are required to be within the ~22.5 kton fiducial volume defined by the volume inset from the ID walls by 2 m. An event whose particles are completely contained within the ID is classified as FC, while an event with particles exiting the ID and depositing energy into the outer detector (OD) is classified as PC. The PC sample is further classified into two

subcategories, PC stopping and PC through-going. The former corresponds to events with a particle that stops in the OD, while in the case of the latter, the particle exits the OD. UPMU events are produced by the charged current interactions of atmospheric muon neutrinos in the rock surrounding the detector. Muons traveling in the upward direction are selected to avoid contamination from cosmic-ray muons. The UPMU stopping sample is defined by events which enter from outside the detector and stop inside the ID, while the UPMU through-going sample is composed of those that enter and subsequently exit the ID. The expected mean energy for each of the event class is ~1 GeV for FC, ~10 GeV for PC, ~10 GeV for UPMU stopping, and ~100 GeV for UPMU through-going. Descriptions of the event reduction and reconstruction can be found in [20].

B. Monte Carlo simulation

In this paper, independent 500 yr Monte Carlo (MC) samples are used for SK-I and SK-II. The analyses use the Honda2006 neutrino flux [21] and neutrino interactions are simulated using the NEUT interaction generator [22,23].

III. OSCILLATION FRAMEWORK

In the following sections we will consider two separate NSI models derived from a more general formalism. We introduce first the more general framework, restricting its scope later to the particular NSI effects we aim to study. The full three-flavor Hamiltonian, $H_{\alpha\beta}$, governing the propagation of neutrinos in the presence of effects from NSI is

$$H_{\alpha\beta} = \frac{1}{2E} U_{\alpha j} \begin{pmatrix} 0 & 0 & 0 \\ 0 & \Delta m^2_{21} & 0 \\ 0 & 0 & \Delta m^2_{31} \end{pmatrix} (U^\dagger)_{k\beta} + V_{\mathrm{MSW}} + \sqrt{2} G_F N_f \begin{pmatrix} \varepsilon_{ee} & \varepsilon_{e\mu} & \varepsilon_{e\tau} \\ \varepsilon_{e\mu} & \varepsilon_{\mu\mu} & \varepsilon_{\mu\tau} \\ \varepsilon_{e\tau} & \varepsilon_{\mu\tau} & \varepsilon_{\tau\tau} \end{pmatrix}. \quad (1)$$

In this equation U is the unitary PMNS matrix [24], which describes standard neutrino mixing as rotations among pairs of mass eigenstates parametrized by unique mixing angles, θ_{ij}. Here the squared difference of the neutrino masses is denoted by Δm^2_{ij}, V_{MSW} is the MSW potential in the flavor basis [13,25], G_F is the Fermi coupling constant, N_f is the fermion number density in matter along the path of the neutrino, and the $\varepsilon_{\alpha\beta}$ represent the NSI coupling parameters. The nonuniversal couplings are represented by the flavor diagonal ε and the FCNC interactions by the off-diagonal elements. Standard neutrino oscillations are recovered when all of the $\varepsilon_{\alpha\beta} = 0$. Note that while the first term of the Hamiltonian carries an explicit energy dependence, the second and third terms do not and instead are functions of the local matter density. For our calculations below we employ the PREM model [26] of the Earth's density profile and chemical composition, where the proton to nucleon ratio in the mantle and core are set to be $Y_p = 0.497$ and 0.468, respectively [27]. In many of our calculations we use the average matter density along the path of the neutrino.

IV. ANALYSIS WITH A TWO-FLAVOR HYBRID MODEL

We consider first a model in which NSI effects in the $\nu_\mu - \nu_\tau$ sector coexist with standard two-flavor $\nu_\mu \leftrightarrow \nu_\tau$ neutrino oscillations. In this scenario all NSI that couple to ν_e in Eq. (1), $\varepsilon_{e\beta}$, are set to zero. Allowing the remaining parameters which couple to ν_μ and ν_τ to be nonzero introduces a matter-dependent effect on the oscillations of $\nu_\mu \leftrightarrow \nu_\tau$. Since the standard two-flavor scenario (θ_{12}, θ_{13}, and $\Delta m^2_{21} = 0$) does not incorporate oscillations into ν_e, there is no separate effect from the standard matter potential, V_{MSW}. Labeling this the *two-flavor hybrid model*, we can explore NSI couplings by searching for matter-induced distortions of standard $\nu_\mu \leftrightarrow \nu_\tau$ oscillations.

A. Formalism

The two-flavor hybrid model can be extracted from Eq. (1) by setting $\Delta m^2_{21} = 0$. Following the formalism of M. C. Gonzalez-Garcia and M. Maltoni [28], assuming that neutrinos possess nonstandard interactions with only d-quarks [17,29], and defining $\varepsilon_{\mu\tau} \equiv \varepsilon$ and $\varepsilon_{\tau\tau} - \varepsilon_{\mu\mu} \equiv \varepsilon'$ the ν_μ survival probability in constant density matter is given by

$$P_{\nu_\mu \to \nu_\mu} = 1 - P_{\nu_\mu \to \nu_\tau} = 1 - \sin^2 2\Theta \sin^2\left(\frac{\Delta m^2_{23} L}{4E} R\right). \quad (2)$$

The effective mixing angle, Θ, and the correction factor to the oscillation wavelength, R, are given by

$$\sin^2 2\Theta = \frac{1}{R^2}(\sin^2 2\theta + R_0^2 \sin^2 2\xi + 2R_0 \sin 2\theta \sin 2\xi),$$
$$R = \sqrt{1 + R_0^2 + 2R_0(\cos 2\theta \cos 2\xi + \sin 2\theta \sin 2\xi)},$$
$$R_0 = \sqrt{2} G_F N_f \frac{4E}{\Delta m^2} \sqrt{|\varepsilon|^2 + \frac{\varepsilon'^2}{4}},$$
$$\xi = \frac{1}{2}\tan^{-1}\left(\frac{2\varepsilon}{\varepsilon'}\right), \quad (3)$$

where θ is the standard two-flavor mixing angle, and ξ is the NSI-induced effective rotation angle in matter. Both the effective mixing angle and the correction factor depend on the neutrino energy as well as the standard oscillation and NSI parameters. These parameters are shown as a function of energy for several values of ε and ε' in Fig. 1.

B. Expected phenomena

Because of the energy dependence of the standard oscillation term in Eq. (1), the relative dominance of NSI in

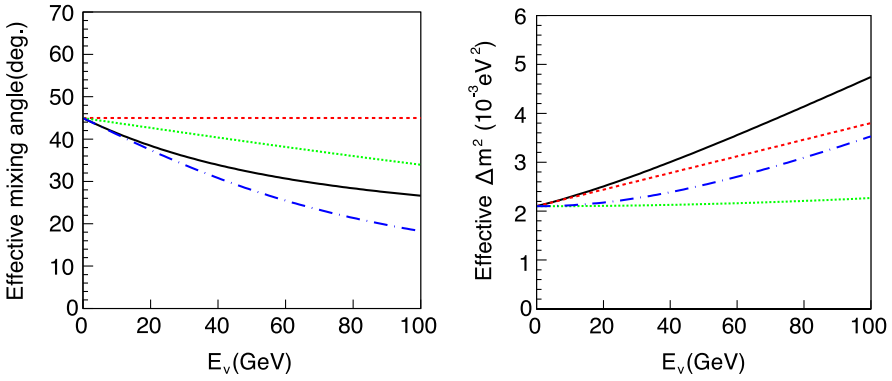

FIG. 1 (color online). (Left) Effective mixing angle in matter. (Right) Effective mass squared difference in matter. In both panels, solid black curves indicate the case with (ε (FCNC), ε'(NU)) = (0.015, 0.05), dashed red curves with (0.015, 0.0), dotted green curves with (0.0, 0.015), dashed-dotted blue curves with (0.0, 0.05). As for the vacuum parameters, $\theta_{23} = 45°$ and $\Delta m^2_{23} = 2.1 \times 10^{-3}$ eV^2 are assumed. Matter density is defined as constant $\rho = 5.0\,\mathrm{g/cm^3}$.

the hybrid model is expected to depend on the neutrino energy. The effects of NSI on neutrino oscillation can be divided into three energy ranges: (1) $E_\nu < 1$ GeV, (2) $1 < E_\nu < 30$ GeV, (3) $E_\nu > 30$ GeV.

(1) $E_\nu < 1$ GeV
At these low energies, the eigenvalue of the vacuum term $\Delta m^2_{23}/2E_\nu (\gtrsim 1 \times 10^{-12}$ eV) is larger than that of the NSI matter term $\sqrt{2} G_F N_f \varepsilon (\sim 1 \times 10^{-13}$ eV), assuming $\Delta m^2_{23} = 2.1 \times 10^{-3}$ eV^2, $N_f \equiv N_d \sim 3N_e$ and $\varepsilon \sim \mathcal{O}(1)$. Thus the $\nu_\mu \rightarrow \nu_\tau$ transition is mostly governed by the standard two-flavor oscillation and there is no significant contribution from NSI. Note that $\varepsilon \sim \mathcal{O}(1)$ is a conservative assumption according to the NuTeV limit $|\varepsilon_{\mu\tau}| < 0.05$ [30].

(2) $1 < E_\nu < 30$ GeV
This energy range corresponds to the FC Multi-GeV (visible energy greater than 1330 MeV), PC, and UPMU stopping samples. In this region the matter term competes with the vacuum term and thus the $\nu_\mu \rightarrow \nu_\tau$ transition is no longer dominated by standard oscillations but is modified by the matter term. The left panel of Fig. 1 shows that for nonzero NU the effective mixing angle decreases with increasing neutrino energy, thereby suppressing $\nu_\mu \rightarrow \nu_\tau$ transitions. Similarly, the right panel shows that nonzero FCNC interactions affect the frequency of oscillations. Since the effective mass splitting, $\Delta m^2_{\mathrm{eff}} \equiv R \Delta m^2_{23}$, is larger than Δm^2_{23}, the first oscillation maximum is expected to occur at higher neutrino energies than for standard oscillations. Focusing on the zenith angle distributions presented in the left panel of Fig. 2, the magnitude of the μ-like deficit in the upward-going direction is expected to become smaller due to ε'. Further, the shape of the zenith angle distribution near and above the horizon is modified in the presence of ε for the higher energy ν_μ samples.

(3) $E_\nu > 30$ GeV
Above 30 GeV, most atmospheric neutrinos are in the UPMU through-going sample, which ranges in energy from tens of GeV to ~100 TeV. At these

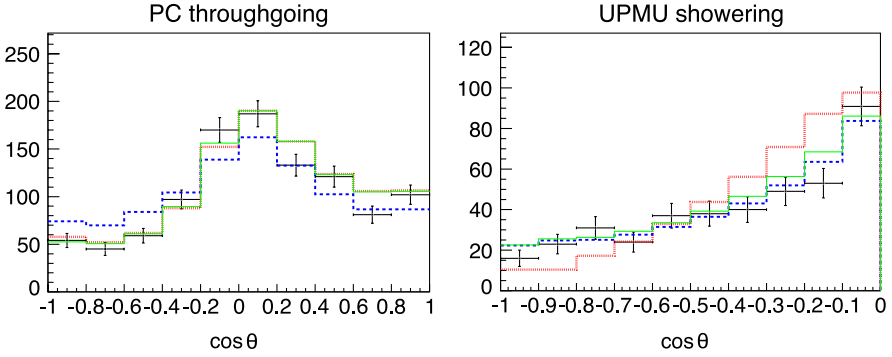

FIG. 2 (color online). Zenith angle distribution for PC through-going (left) and UPMU showering (right, included in UPMU through-going where energy loss of muon is caused by pair production, Bremsstrahlung, and photonuclear interactions) subsamples. In the solid green line (ε, ε') = (1.0×10^{-3}, -2.4×10^{-2}), in the dashed blue line (1.0×10^{-3}, -0.38), and in the dotted red line (3.2×10^{-3}, -2.4×10^{-2}). In all lines the standard oscillation parameters are $\theta_{23} = 45°$ and $\Delta m^2_{23} = 2.1 \times 10^{-3}$ eV^2.

energies vacuum oscillations have less of an effect on the $\nu_\mu \rightarrow \nu_\tau$ transition, while the transitions induced by the matter term become significant when the neutrino path length in the Earth is sufficiently long. As shown in the right panel of Fig. 2, FCNC interactions play a leading role in this energy range because the modified oscillation frequency is comparable in size to the oscillation frequency of these neutrinos in the Earth. Thus, $\nu_\mu \rightarrow \nu_\tau$ transitions driven by FCNC are expected to occur. In contrast, at these energies NU interactions suppress the effective mixing angle and therefore are expected to produce a subleading effect on the data. Note that at the current values of the atmospheric mixing parameters, the standard $\nu_\mu \rightarrow \nu_\tau$ transition is already increasingly suppressed at these energies. In summary, FCNC interactions induce a faster oscillation frequency and lead to $\nu_\mu \rightarrow \nu_\tau$ transitions at shorter path lengths in matter, while NU suppresses the transition even at these energies.

C. Analysis method

We evaluate the agreement between the data and Monte Carlo oscillated according to the hybrid NSI model using a χ^2 test. The SK-I and SK-II data are divided according to their reconstructed event types, momenta, and zenith angles into 400 and 350 bins, respectively. In SK-I (SK-II) there are 310 (280) bins for the FC samples, 60 (40) for the PC samples, and 30 (30) for the upward-going muon samples. Data from the two run periods are treated separately due to differences in the detector response and in the effects on the atmospheric neutrino flux from solar modulations during the runs. In order to accurately treat bins with small statistics in this binning scheme, a likelihood based on Poisson probabilities [31] is used. The complete χ^2 with 750 data bins and 90 systematic uncertainties is defined as

$$\chi^2 = 2\sum_{i=1}^{750}\left(N_i^{\rm exp}\left(1+\sum_{j=1}^{90} f_j^i \epsilon_j\right) - N_i^{\rm obs} + N_i^{\rm obs}\ln\frac{N_i^{\rm obs}}{N_i^{exp}(1+\sum_{j=1}^{90} f_j^i \epsilon_j)}\right) + \sum_{j=1}^{90}\left(\frac{\epsilon_j}{\sigma_j^{\rm sys}}\right)^2, \quad (4)$$

where ϵ_j is a fitting parameter for the j-th systematic error and f_j^i is the fractional change of the event rate in the i-th bin due to a 1σ change in j-th systematic error. The systematic errors cover uncertainties in the neutrino flux, their interactions, and in the response of the detector. A summary of these errors and their fitted error parameters are presented in the Appendix.

Using this equation, a value of χ^2 is evaluated at each point in a four-dimensional parameter space defined by $\sin^2 2\theta_{23}$, Δm^2_{23}, $\log_{10}\varepsilon$, and $\log_{10}\varepsilon'$, where ε and ε' range from 1.0×10^{-3} to 3.2×10^{-2} and from 1.0×10^{-3} to 0.42, respectively. The fit is performed on a $51\times51\times51\times51$ grid in this space. In Eq. (4), the ϵ_j parameters are varied to minimize the value of χ^2 for each choice of oscillation parameters. The point in parameter space returning the smallest value of χ^2 is defined as the best fit. Since the effects of ε are symmetric between negative and positive values, we only consider positive ε.

D. Two-flavor nonstandard interaction analysis result

The result of a scan on this parameter space gives a best fit at

$$\sin^2 2\theta_{23} = 1.00, \qquad \Delta m^2_{23} = 2.2\times10^{-3}\ {\rm eV}^2,$$
$$\varepsilon = 1.0\times10^{-3}, \qquad \varepsilon' = -2.7\times10^{-2} \quad (5)$$
$$\chi^2_{\rm min} = 838.9/746.0\ {\rm d.o.f.}$$

The best-fit systematic error parameters for the best-fit point are summarized in the Appendix.

Figure 3 shows the allowed neutrino oscillation parameter regions, $\sin^2 2\theta_{23}$ and Δm^2_{23}, from this analysis and from the standard oscillation analysis. The three contours correspond to the 68%, 90% and 99% C.L., defined by $\chi^2 = \chi^2_{\rm min} + 2.30$, 4.61, and 9.21, respectively. There is no inconsistency between the two sets of allowed regions. Since the difference in the minimum χ^2 values is not large, no significant contribution to standard two-flavor oscillations from NSI effects is found in this analysis.

The allowed regions of the NSI parameters are shown in Fig. 4, where the undisplayed parameters $\sin^2 2\theta_{23}$ and Δm^2_{23} have been minimized over. At 90% C.L. the obtained limits on the NSI parameters in the $\nu_\mu - \nu_\tau$ sector are

$$|\varepsilon| < 1.1\times10^{-2} \text{ and } -4.9\times10^{-2} < \varepsilon' < 4.9\times10^{-2}. \quad (6)$$

These limits can be compared with a phenomenological study of the SK-I (79 kton yr) and MACRO

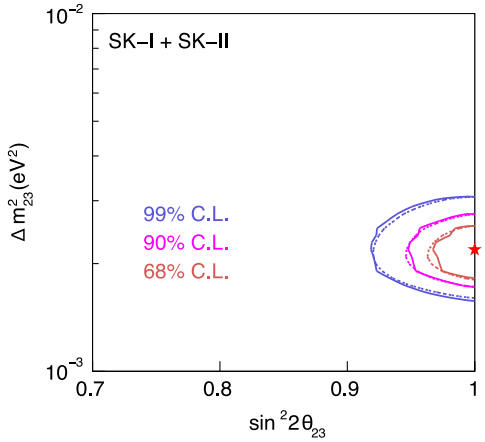

FIG. 3 (color online). Allowed oscillation parameter regions derived by the two-flavor hybrid model analysis (solid curves), where the undisplayed parameters ε and ε' are integrated out. For reference, the result of standard two-flavor oscillation is added (dashed curves).

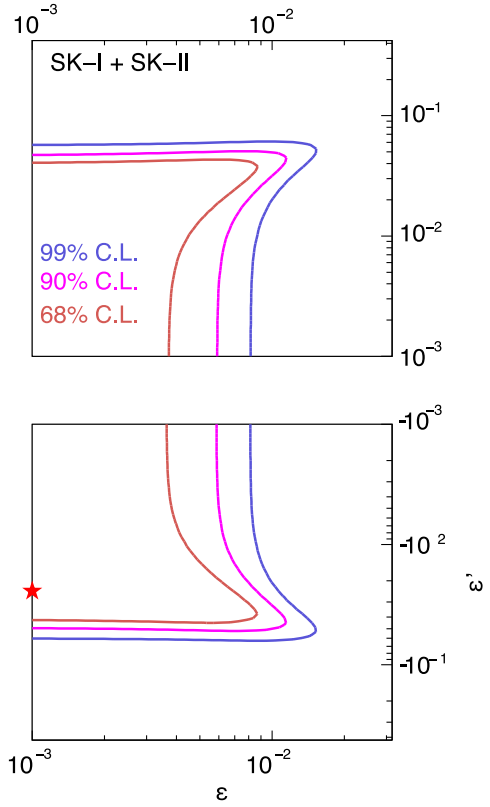

FIG. 4 (color online). Allowed NSI parameter regions in the two-flavor hybrid model. The horizontal axis shows ε (FCNC) and the vertical axis shows ε' (NU). Undisplayed parameters $\sin^2 2\theta_{23}$ and Δm^2_{23} are integrated out. The star represents the best-fit point for the NSI parameters.

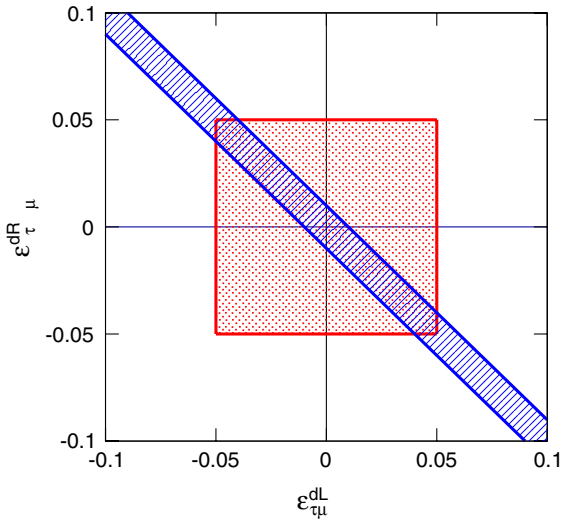

FIG. 5 (color online). Constraints on NSI parameters. The blue hatched area indicates the allowed parameter region obtained in this analysis while the red square region denotes the limit from the NuTeV experiment [30]. Both areas show the 90% C.L.

atmospheric neutrino data [17], in which limits on FCNC and NU at 90% C.L. are estimated to be $2.0 \times 10^{-2} < \varepsilon < 1.3 \times 10^{-2}$ and $-4.7 \times 10^{-2} < \varepsilon' < 4.2 \times 10^{-2}$.

The most stringent constraints on $\varepsilon(\equiv \varepsilon_{\mu\tau})$ are from the NuTeV experiment [30],

$$|\varepsilon^L_{\mu\tau}| < 0.05, |\varepsilon^R_{\mu\tau}| < 0.05, \quad (7)$$

where L and R denotes left-handed and right-handed fermions with which neutrinos collide.

Since measurements of NSI using atmospheric neutrinos cannot distinguish between interactions on left-handed and right-handed fermions, we parametrize NSI in this analysis as $\varepsilon_{\alpha\beta} = \varepsilon^L_{\alpha\beta} + \varepsilon^R_{\alpha\beta}$. To account for differences in the detection approaches, the SK constraints are compared to the NuTeV limits in the two-dimensional space of $\varepsilon^{dL}_{\alpha\beta}$ and $\varepsilon^{dR}_{\alpha\beta}$ in Fig. 5.

To check for the existence of a possible fitting bias in the χ^2 method discussed above we performed 3000 toy MC experiments assuming the NSI parameters from the fit to the data (Eq. (5) are the true values). Each toy MC data set is generated by smearing the MC prediction at these values following Poisson statistics. The toy MC is then fit against the MC prediction across the entire oscillation parameter space and a best fit is computed. Among the 3000 toy MC the majority of best fits fell on the assumed true value suggesting no particular fitting bias. An examination of the distributions of the fitted error parameters similarly shows no irregularities. Since the analysis framework here is essentially the same as the model presented in Sec. V D, this conclusion is applicable to that discussion as well.

E. Discussion

As described in Sec. IV B, NSI are expected to affect multi-GeV muon neutrinos, and are consequently constrained by the Super-K μ-like samples. Figure 6 shows the allowed region spanned by the NSI parameters for three subsamples of the data. Since the minimum χ^2 is located in negative ε' space, the negative ε' plane is presented. The strongest constraint on ε comes from the UPMU through-going sample (solid curve), while ε' is most tightly constrained by the PC and UPMU stopping (dashed curve) samples. The constraint from the sub-GeV samples is too weak to be visible in this figure.

These constraints on ε can be understood as follows. As shown in the right panel of Fig. 1, FCNC interactions (dashed red curve) increase the effective neutrino oscillation frequency thereby shortening the oscillation length for neutrinos at a fixed energy. Above 30 GeV, where the atmospheric sample is dominated by UPMU events, the oscillation length in the absence of NSI is already greater than the diameter of the Earth. The addition of FCNC effects on the other hand can shorten the oscillation length enough to induce oscillations in the steepest upward-going bins of the UPMU sample. This is an apparent contradiction with the data and results in a tight constraint on ε. Below $\sim$30 GeV, the oscillation length is sufficiently

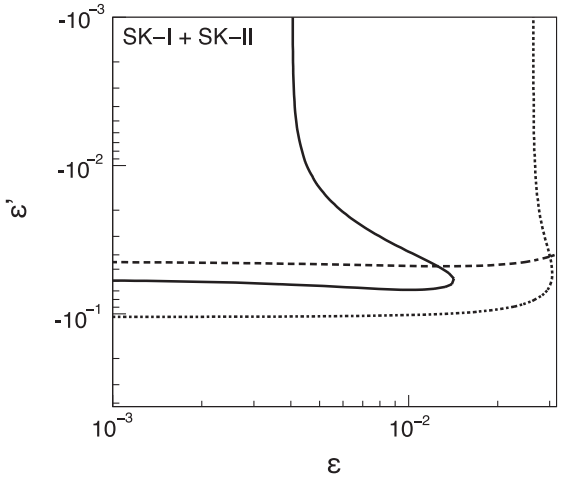

FIG. 6. Allowed NSI parameter regions for various event subsamples. The solid curve indicates the allowed region from the UPMU through-going sample, the dashed curve is that from the PC and UPMU stopping samples, and the dotted curve is from the FC Single-ring Multi-GeV and Multi-ring samples. Each contour corresponds to $\chi^2 = \chi^2 + 2.30$ (68% C.L.).

short in both standard and NSI cases to cause oscillations in the FC and PC samples. For this reason it is more difficult for these samples to discriminate between standard- and FCNC-induced oscillations.

As for the most stringent limit on NU provided by the PC and UPMU stopping samples note that a large ε' induces a smaller μ-like deficit in the upward-going direction relative to standard oscillations. In addition, a distortion of the zenith angle distribution near and above the horizon is predicted (see dashed blue line in the left panel of Fig. 2). Since the SK data from these samples are already consistent with standard oscillations, a tight constraint on NSI is obtained. Limits on NU provided other subsamples can similarly be understood from the discussion in Sec. IV B.

V. ANALYSIS WITH A THREE-FLAVOR HYBRID MODEL

We now consider a *three-flavor hybrid model* in which NSI in the $\nu_e - \nu_\tau$ sector coexist with standard two-flavor $\nu_\mu \leftrightarrow \nu_\tau$ oscillations and all other NSI are zero. By introducing couplings between ν_e and ν_τ, this model allows flavor transitions of all types. That is, an overall $\nu_\mu \rightarrow \nu_e$ transition becomes possible due to the $\varepsilon_{e\tau}$ induced $\nu_\tau \rightarrow \nu_e$ conversion working in conjunction with the standard $\nu_\mu \leftrightarrow \nu_\tau$ oscillation:

$$\nu_\mu \xrightarrow{\theta_{23}} \nu_\tau \xrightarrow{\varepsilon_{e\tau}} \nu_e. \tag{8}$$

Note that since the other FCNC epsilons have been set to zero, there is no direct transition between ν_μ and ν_e. This analysis therefore aims to constrain possible NSI effects by examining changes in the ν_e and ν_μ fluxes on top of standard oscillationlike effects.

A. Formalism

An evolution matrix from time t_0 to t can be obtained by diagonalizing the Hamiltonian in Eq. (1) in terms of the leptonic mixing matrix in matter U' and the effective eigenvalues $\hat{H} = \mathrm{diag}(E_1, E_2, E_3)$. In the case of constant matter density, the evolution matrix in natural units is

$$S_{\beta\alpha}(t, t_0) = \sum_{i=1}^{3} (U'_{\alpha i})^* U'_{\beta i} \mathrm{e}^{-iE_i(t-t_0)}, \quad \alpha, \beta = e, \mu, \tau. \tag{9}$$

Thus the neutrino oscillation probability under the effect of NSI can be expressed as

$$P_{\alpha\beta} = |S_{\beta\alpha}(t, t_0)|^2. \tag{10}$$

An analytical calculation of Eq. (10) is presented in other documents, for example [36]. In this work we derive the oscillation probabilities by numerically solving the matrix in Eq. (10) where, in order to account for the varying matter density in the Earth (from 2.5 to 13 g/cm^3), the neutrino path is divided into several constant density steps and the evolution matrix in each is calculated.

B. Expected phenomena

As in the two-flavor hybrid model, the effects of NSI are expected to vary with the neutrino energy. We consider three energy ranges: (1) $E_\nu < 1$ GeV, (2) $1 < E_\nu < 15$ GeV, and (3) $E_\nu > 15$ GeV.

(1) $E_\nu < 1$ GeV
Since the standard oscillation eigenvalue $\Delta m^2/2E_\nu$ is much greater than the matter potential $\sqrt{2}G_F N_d$, $\nu_\mu \rightarrow \nu_\tau$ transitions induced by these oscillations are expected to be dominant and the effects from NSI can be ignored.

(2) $1 < E_\nu < 15$ GeV
In this energy range, the matter term has a sizable effect on the $\nu_\mu \rightarrow \nu_\tau$ transition as it did in the two-flavor hybrid model. Moreover, since the current limits on the NSI parameters governing $\nu_e \rightarrow \nu_\tau$ transitions are poor, $\varepsilon_{e\tau} \sim \mathcal{O}(10^{-1})$ [30], large effects from NSI are possible.
The modification of the ν_e flux by NSI can be parametrized by two oscillation probabilities: $P(\nu_e \rightarrow \nu_e)$ and $P(\nu_\mu \rightarrow \nu_e)$ in Eq. (8). Normalizing by the ν_e flux(Φ_e), and disregarding any ν_μ contamination, the resulting e-like distributions can be approximately expressed as $P(\nu_e \rightarrow \nu_e) + rP(\nu_\mu \rightarrow \nu_e)$, where $r \equiv \Phi_\mu/\Phi_e$ is the neutrino

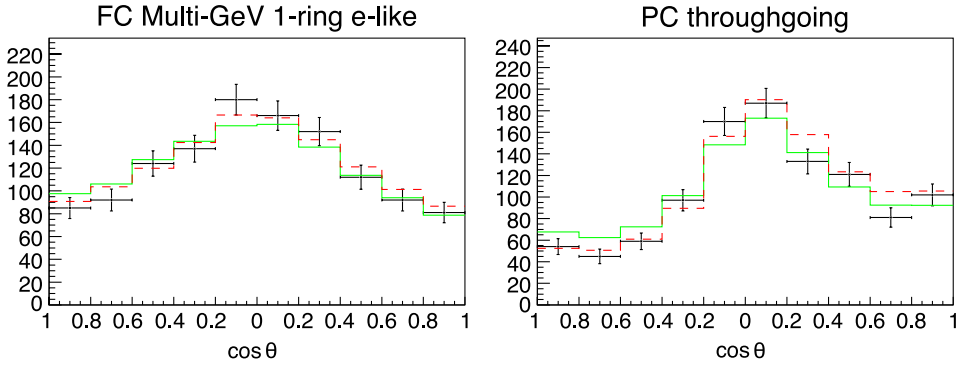

FIG. 7 (color online). Zenith angle distribution for typical e-like (left, FC Multi-GeV 1-ring e-like) and μ-like (right, PC through-going) samples. The solid green line is the MC prediction at $\varepsilon_{ee} = 0.0$, $\varepsilon_{e\tau} = 0.2$, and $\varepsilon_{\tau\tau} = 0.2$. The dashed red line is that for standard neutrino oscillations. In all lines the standard oscillation parameters are $\theta_{23} = 45°$ and $\Delta m^2_{23} = 2.1 \times 10^{-3}$ eV^2.

flavor ratio [37]. This ratio grows with increasing neutrino energy and though it is highly dependent on the neutrino zenith angle, near the horizon it is $\sim$2 up to around 10 GeV. Thus, if $P(\nu_e \to \nu_e) + rP(\nu_\mu \to \nu_e) \lesssim 1$, as is the case when $\varepsilon_{e\tau}$ and $\varepsilon_{\tau\tau}$ have comparable values, then since $P(\nu_e \to \nu_e)$ is suppressed by $\varepsilon_{e\tau}$ and $P(\nu_\mu \to \nu_e)$ by $\varepsilon_{\tau\tau}$, the number of e-like events at the horizon can be expected to decrease. In contrast, the number of e-like events in the upward-going bins would effectively increase because large values of $\varepsilon_{e\tau}$ produce additional ν_e from ν_τ created during standard oscillations. This effect is enhanced by the larger flavor ratio in these regions and enables the multi-GeV

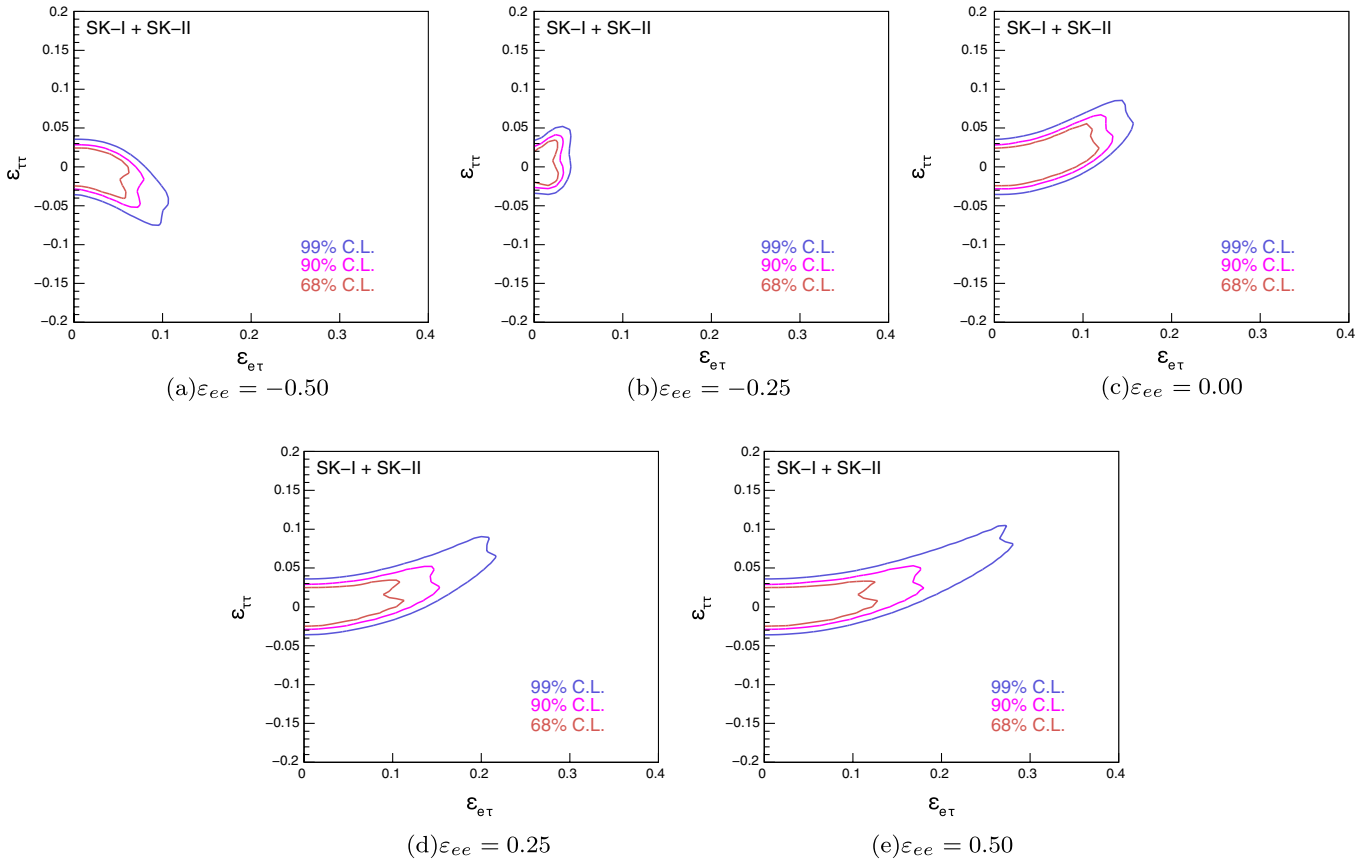

FIG. 8 (color online). Allowed NSI parameter regions at fixed ε_{ee} at 68%, 90% and 99% C.L., where contours are drawn at $\chi^2 - \chi^2_{\rm min} = 2.30$, 4.61 and 9.21, respectively.

e-like samples to help constrain $\varepsilon_{e\tau}$. These effects are shown in the left panel of Fig. 7.

Effects driven by $\varepsilon_{\tau\tau}$ on the other hand may be described in terms of the limiting case where the other NSI are set to zero. In this case the problem reduces to the two-flavor hybrid model with $\varepsilon = 0$ and $\varepsilon' = \varepsilon_{\tau\tau}$. Therefore a constraint on ϵ' similar to that from the two-flavor case can be expected.

(3) $E_\nu > 15$ GeV

Above a few tens of GeV the ν_e flux decreases as their parent muons increasingly reach the ground before decaying, making it possible to neglect the ν_e contribution to the ν_μ flux from oscillations induced by $\varepsilon_{e\tau}$. Conversely, changes in that flux can be clearly recognized as NSI-driven $\nu_\tau \rightarrow \nu_e$ conversion at these energies. As in the two-flavor hybrid case, $\varepsilon_{\tau\tau}$ can be expected to suppress the effective mixing angle and increase the effective mass splitting in the $\nu_\mu \rightarrow \nu_\tau$ sector. Both of these effects can be seen in the right panel of Fig. 7.

As pointed out in Ref. [38] the atmospheric neutrino sample cannot effectively constrain ε_{ee}. This is due to the fact that when $\varepsilon_{e\tau}$ is zero, the eigenstates of the Hamiltonian in matter are identical to the vacuum eigenstates. In this case, the matter eigenvalues are no longer dependent upon ε_{ee} and the problem reduces to two-flavor NSI mixing with $\nu_\mu \leftrightarrow \nu_\tau$ transitions in matter modified by only $\varepsilon_{\tau\tau}$. Despite the lack of sensitivity to ε_{ee}, at fixed nonzero values it dictates a parabolic relationship among the NSI parameters, which in the limit where one of the matter eigenvalues is small takes the form

$$\varepsilon_{\tau\tau} \sim \frac{3|\varepsilon_{e\tau}|^2}{1 + 3\varepsilon_{ee}}. \tag{11}$$

TABLE I. The allowed NSI parameters at the 90% C.L. as a function of ε_{ee}.

ε_{ee}	Best-fit $\varepsilon_{e\tau}$	Best-fit $\varepsilon_{\tau\tau}$	Minimum χ^2
−0.50	0.016	−0.016	831.1
−0.25	0.016	0.024	829.9
0.00	0.024	0.016	830.9
0.25	0.000	−0.016	831.4
0.50	0.000	−0.016	831.4

This is a general feature which will present itself in the shape of our allowed regions below.

C. Analysis method

The analysis procedure for the three-flavor hybrid model follows that used for the two-flavor hybrid model. A value of χ^2 is evaluated at each grid point in the three-dimensional parameter space of ε_{ee}, $\varepsilon_{e\tau}$ and $\varepsilon_{\tau\tau}$, where 51 points are chosen for each. Since $\varepsilon_{e\tau}$ enters the oscillation equations as $|\varepsilon_{e\tau}|$ [38] when θ_{13} and solar oscillations (Δm^2_{12} and θ_{12}) are not considered, we only test positive values of the parameter.

We first set the standard two-flavor parameters to $(\sin^2\theta_{23}, \Delta m^2) = (0.5, 2.1 \times 10^{-3}\ \mathrm{eV}^2)$ as motivated by the results from the two-flavor hybrid model and other Super-K analyses [39]. Here the standard oscillation parameters are taken as fixed values. This assumption will be verified later by comparing the allowed NSI parameter regions derived using slightly different standard oscillation parameters. Modifications to the fitting results when θ_{13} is nonzero are presented in Sec. VI.

D. Results of the three-flavor NSI analysis

The allowed regions for the three-flavor NSI parameters are shown in Fig. 8. Allowed regions for five fixed values

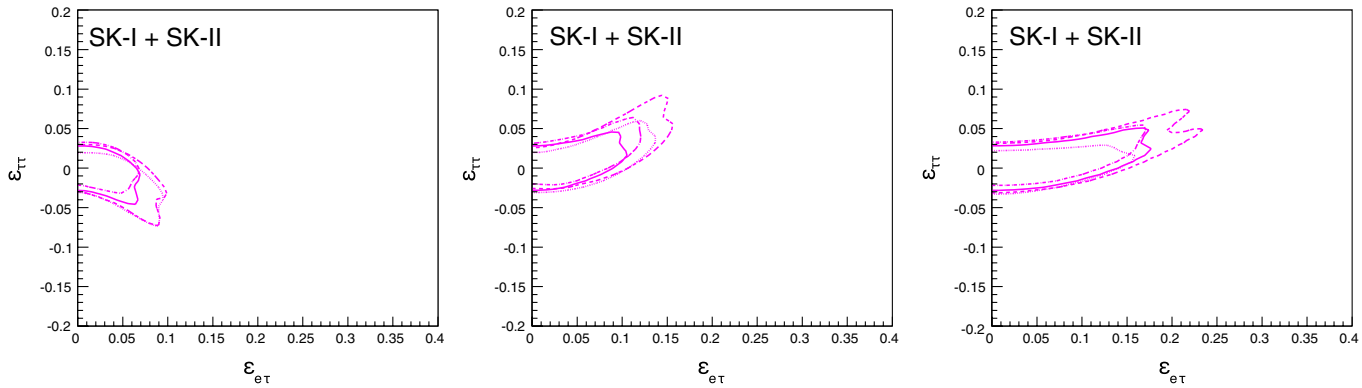

(a)$\varepsilon_{ee} = -0.50$ (b)$\varepsilon_{ee} = 0.00$ (c)$\varepsilon_{ee} = 0.50$

FIG. 9 (color online). Allowed NSI parameter regions in the $\varepsilon_{e\tau}$ vs $\varepsilon_{\tau\tau}$ plane at the 90% C.L. for $\varepsilon_{ee} = -0.5$, 0.0, and 0.5 using four sets of standard oscillation parameters. The solid curve corresponds to $(\sin^2\theta_{23}, \Delta m^2) = (0.5, 1.7 \times 10^{-3}\ \mathrm{eV}^2)$, the dashed curve to $(0.5, 2.7 \times 10^{-3}\ \mathrm{eV}^2)$, the dotted curve to $(0.39, 2.1 \times 10^{-3}\ \mathrm{eV}^2)$, and the dashed-dotted curve to $(0.61, 2.1 \times 10^{-3}\ \mathrm{eV}^2)$.

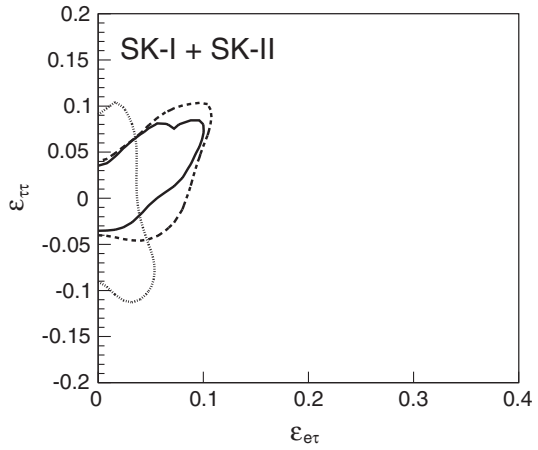

FIG. 10. Allowed NSI parameter regions at 90% C.L. derived for three subsamples at $\varepsilon_{ee} = -0.25$. The solid curve indicates the allowed region given by the UPMU through-going sample, the dashed curve shows the PC and UPMU stopping sample, and the dotted curve is the constraint from the FC multi-GeV samples.

of ε_{ee} (-0.50, -0.25, 0.00, 0.25, and 0.50) are presented. The three contours correspond to the 68%, 90% and 99% C.L. regions as defined by $\chi^2 = \chi^2_{\rm min} + 2.30$, 4.61, and 9.21, respectively. The best-fit values for each value of ε_{ee} are summarized in Table I, and the systematic error parameters at the best-fit point for $\varepsilon_{ee} = -0.25$ are presented in the Appendix.

In these figures, except for the projection for $\varepsilon_{ee} = -0.25$, parabola-like regions in the $\varepsilon_{e\tau}$–$\varepsilon_{\tau\tau}$ are shown. In particular, the allowed region extends to negative $\varepsilon_{\tau\tau}$ values when $\varepsilon_{ee} = -0.5$, while they extend to the positive values above $\varepsilon_{ee} = 0$. This feature is consistent with a transition of the matter eigenvalue hierarchy discussed in Ref. [38].

Next, we evaluate the influence of using fixed standard oscillation parameters. Figure 9 shows the allowed NSI parameter regions using four slightly different sets of standard oscillation parameters. The oscillation parameters are taken from the 90% C.L. allowed region from the standard SK two-flavor analysis. Although slight changes appear when the NSI fits are repeated using these parameters, their minimum χ^2 values are larger than that of the original fit by less than 1.5 units. Therefore no significant change in the allowed parameter regions is expected even if the standard oscillation parameters are allowed to vary during the NSI fit. Finally note that the current allowed regions of $\sin^2\theta_{23}$ and Δm^2 are constrained more tightly by analyses using the full SK data set, which is larger than the sample used here.

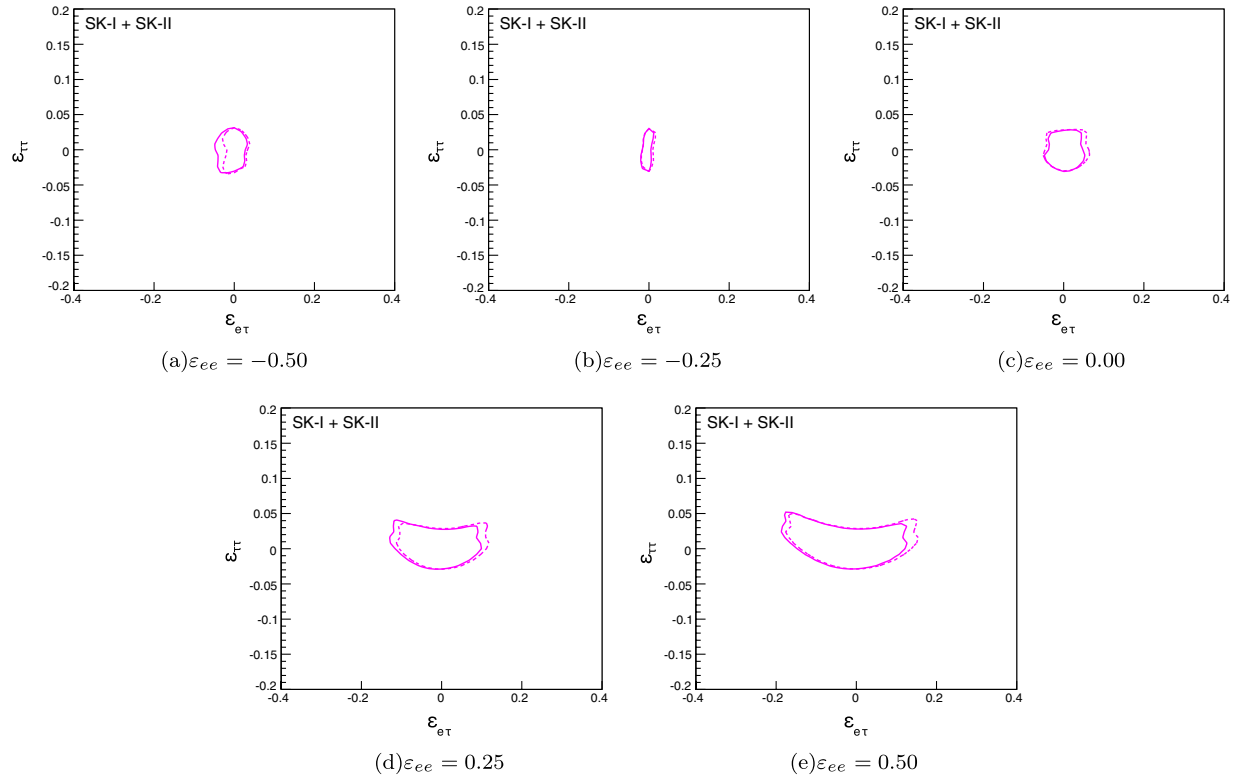

(a)$\varepsilon_{ee} = -0.50$ (b)$\varepsilon_{ee} = -0.25$ (c)$\varepsilon_{ee} = 0.00$

(d)$\varepsilon_{ee} = 0.25$ (e)$\varepsilon_{ee} = 0.50$

FIG. 11 (color online). Allowed NSI parameters regions in the $\varepsilon_{e\tau}$ vs $\varepsilon_{\tau\tau}$ plane at the 90% C.L. when $\sin^2\theta_{13} = 0.04$. The solid curve and dashed curve indicate the normal inverted hierarchy fits, respectively.

E. Discussion

Figure 10 shows the allowed parameter regions for three subsets of the atmospheric sample. The high energy ν_μ-rich UPMU through-going sample (indicated by the solid curve) and PC + UPMU stopping samples constrain $\varepsilon_{\tau\tau}$ as expected. However, these samples provide no significant contribution to the constraint on $\varepsilon_{e\tau}$ because they lack an e-like component. On the other hand, the FC multi-GeV samples (shown by the dotted curve) include several e-like subsamples which better constrain $\varepsilon_{e\tau}$.

TABLE II. Systematic errors in the two-flavor hybrid model analysis coming from uncertainties in the neutrino flux, neutrino interactions, and particle production models. These are common to all SK geometries. The second column shows the best-fit value of the systematic error parameter ϵ_j in percent and the third column shows the estimated $1-\sigma$ error size in percent.

Systematic Uncertainties in Neutrino Flux and Neutrino Interactions	Fit (%)	σ (%)
Flux normalization ($E_\nu < 1$ GeV)	34.3	25[a]
Flux normalization ($E_\nu > 1$ GeV)	20.6	20[b]
ν_μ/ν_e ($E_\nu < 1$ GeV)	−0.66	2
ν_μ/ν_e ($1 < E_\nu < 10$ GeV)	−1.33	3
ν_μ/ν_e ($E_\nu > 10$ GeV)	7.01	5[c]
$\bar{\nu}_e/\nu_e$ ($E_\nu < 1$ GeV)	3.12	5
$\bar{\nu}_e/\nu_e$ ($1 < E_\nu < 10$ GeV)	1.15	5
$\bar{\nu}_e/\nu_e$ ($E_\nu > 10$ GeV)	−0.90	8[d]
$\bar{\nu}_\mu/\nu_\mu$ ($E_\nu < 1$ GeV)	−0.30	2
$\bar{\nu}_\mu/\nu_\mu$ ($1 < E_\nu < 10$ GeV)	−0.18	6
$\bar{\nu}_\mu/\nu_\mu$ ($E_\nu > 10$ GeV)	1.16	6[e]
Up/down ratio	−0.49	1
Horizontal/vertical ratio	0.51	1
K/π ratio in flux	−5.99	10[f]
Neutrino path length	1.17	10
Sample-by-sample (FC multi-GeV)	−5.67	5
Sample-by-sample (PC + UPMU stopping μ)	−10.1	5
M_A in CCQE and single-π	0.89	10
CCQE cross section	4.49	1[g]
CCQE $\bar{\nu}/\nu$	10.1	1[g]
CCQE ν_μ/ν_e	4.27	1[g]
Single-π cross section	−2.12	20
Single-π π^0 /charged-π	−37.1	40
Single-π $\bar{\nu}/\nu$	−3.09	1[h]
DIS (low-Q^2)	1.26	1[i]
DIS	1.30	5
Coherent-π	15.4	100
NC/CC ratio	−23.9	20
Nuclear effects in ^{16}O nucleus	−24.2	30
Nuclear effects in pion spectrum	10.8	1[j]
ν_τ contamination	−10.9	30
NC in FC μ-like (hadron simulation)	−3.72	10

[a]Uncertainty linearly decreases with logE_ν from 25%(0.1 GeV) to 7%(1 GeV).
[b]Uncertainty is 7% up to 10 GeV, linearly increases with logE_ν from 7%(10 GeV) to 12%(100 GeV) and then to 20%(1 TeV)
[c]Uncertainty linearly increases with logE_ν from 5%(30 GeV) to 30%(1 TeV).
[d]Uncertainty linearly increases with logE_ν from 8%(100 GeV) to 20%(1 TeV).
[e]Uncertainty linearly increases with logE_ν from 6%(50 GeV) to 40%(1 TeV).
[f]Uncertainty increases linearly from 5% to 20% between 100 GeV and 1 TeV.
[g]Difference from the Nieves [32] model is set to 1.0.
[h]Difference from the Hernandez [33] model is set to 1.0.
[i]Difference from CKMT [34] parametrization is set to 1.0.
[j]Difference between NEUT [22,23] and NUANCE [35] is set to 1.0.

VI. ANALYSIS WITH A THREE-FLAVOR HYBRID MODEL WITH NONZERO θ_{13}

There are several scenarios in which subdominant effects from standard neutrino oscillations may affect the allowed NSI parameters. In this section we consider how our limits change when effects from nonzero θ_{13} are included in the analysis.

Present data suggest that θ_{13} is small relative to the other mixing angles, θ_{23} and θ_{12}. The Chooz experiment has placed the most stringent limit on the parameter, indicating that $\sin^2\theta_{13} < 0.04$ [40]. Because of its small size its effects were ignored in the main analysis. However, θ_{13} is expected to induce $\nu_\mu \rightarrow \nu_e$ transitions at multi-GeV energies possibly producing an excess of ν_e that could be misinterpreted as the effect of $\varepsilon_{e\tau}$. Here the analysis of Sec. V is repeated for the normal hierarchy, $\Delta m^2_{23} > 0$, and inverted hierarchy, $\Delta m^2_{23} < 0$, with θ_{13} fixed at the Chooz limit. Including θ_{13} breaks the positive-negative symmetry of $\varepsilon_{e\tau}$ so the fit is expanded to cover both regions. The results of the fit are again presented as a function of ε_{ee} in Fig. 11.

Focusing on the normal hierarchy, the addition of θ_{13} to the fit tends to improve the constraint on $\varepsilon_{e\tau}$. The $\nu_\mu \rightarrow \nu_e$ oscillation probability in constant density matter is proportional to $\sin^2\Theta_{13}$, where Θ_{13} is the effective θ_{13} mixing angle given by,

$$\Theta_{13} \sim \theta_{13} + \phi, \qquad \tan 2\phi \sim \frac{a \sin 2\theta_{13}}{\Delta m^2_{31} - a \cos 2\theta_{13}}. \quad (12)$$

In this equation a is the product of the MSW matter potential and the neutrino energy, $\pm 2\sqrt{2} G_F N_e E_\nu$, where the sign is positive (negative) for neutrinos (antineutrinos). The structure of the denominator can create a resonant enhancement of the oscillation probability depending

TABLE III. Detector related systematic errors, including uncertainties from the event reduction and reconstruction from the two-flavor hybrid analysis. The systematic errors and their resulting fit differ between SK-I and SK-II. The second (fourth) column shows the fitted value of the systematic error parameter in percent for SK-I (SK-II) and the third (fifth) column shows the associated error size in percent.

Systematic Uncertainties in Event Selection	SK-I Fit (%)	SK-I σ (%)	SK-II Fit (%)	SK-II σ (%)
FC reduction	0.03	0.2	<0.01	0.19
PC reduction	−0.81	2.4	−2.56	4.8
FC/PC separation	−0.10	0.6	0.06	0.5
PC stopping/through separation (top)	11.5	15	−18.0	19
PC stopping/through separation (barrel)	−0.60	7.4	−22.2	14
PC stopping/through separation (bottom)	−7.32	11.3	−19.5	18
Non-ν_e BG in Multi-GeV single-ring e-like	0.53	14.5	−6.49	20.6
Non-ν_e BG in Multi-GeV multi-ring e-like	−7.69	39.6	7.18	12.6
Multi-GeV multi-ring e-like	0.28	7	1.12	3.2
Non-ν BG (flasher)	0.12	0.5	−0.11	0.5
Non-ν BG (cosmic-ray muon)	−0.14	0.1	0.23	0.1
Fiducial volume	−0.28	2	0.18	2
Ring separation	5.81	10	−9.33	10
Particle identification	−0.06	1	0.18	1
Particle identification (Multi-ring)	5.86	10	4.83	10
Energy scale calibration	0.07	1.1	−1.71	2.5
Up/down asymmetry of energy calibration	0.09	0.6	−0.18	0.6
UPMU reduction	0.29	1	0.31	1
UPMU stopping/through-going separation	−0.03	0.39	−0.01	0.41
Energy cut for UPMU stopping	−0.08	0.8	−0.04	1.1
UPMU nonshowering/showering separation	−2.02	2.8	−0.49	1.8
BG subtraction of UPMU stopping	3.29	17	−16.5	24
BG subtraction of UPMU nonshowering	−0.08	1.5	1.75	3
BG subtraction of UPMU showering	4.93	13	4.04	24
Sub-GeV 1-ring π^0 selection	−3.11	10	−5.45	10
Sub-GeV 2-ring π^0	−0.50	2	−0.54	2
Decay-e tagging	0.73	1.1	−0.72	1.1
Decay-e π^+-decay uncertainty	−7.63	10	−7.62	10
Solar activity	4.01	20	30.4	50

upon the energy of the neutrino and the density of matter it traverses. If θ_{13} is nonzero, the upward-going ν_e flux is expected to increase in the 2–10 GeV range, coinciding with the region where $\varepsilon_{e\tau}$ can enhance the ν_e flux. Accordingly, part of the ν_e flux induced by $\varepsilon_{e\tau}$ is now occupied by events from θ_{13} transitions which therefore results in a tighter constraint on the parameter. However, the resonance behavior of Eqn. (12) is contingent upon the signs of the mass hierarchy and MSW matter potential. This, coupled with unequal neutrino and antineutrino fluxes in the atmospheric data, results in the asymmetric constraint on $\varepsilon_{e\tau}$ seen in Fig. 11.

TABLE IV. Systematic errors in the three-flavor hybrid model analysis coming from uncertainties in the neutrino flux, neutrino interactions, and particle production models. These are common to all SK geometries. The second column shows the best-fit value of the systematic error parameter ϵ_j in percent and the third column shows the estimated $1-\sigma$ error size in percent.

Systematic Uncertainties in Neutrino flux and neutrino interactions	Fit (%)	σ (%)
Flux normalization ($E_\nu < 1$ GeV)	35.0	25[a]
Flux normalization ($E_\nu > 1$ GeV)	19.3	20[b]
ν_μ/ν_e ($E_\nu < 1$ GeV)	−0.56	2
ν_μ/ν_e ($1 < E_\nu < 10$ GeV)	−1.95	3
ν_μ/ν_e ($E_\nu > 10$ GeV)	4.68	5[c]
$\bar{\nu}_e/\nu_e$ ($E_\nu < 1$ GeV)	2.89	5
$\bar{\nu}_e/\nu_e$ ($1 < E_\nu < 10$ GeV)	1.07	5
$\bar{\nu}_e/\nu_e$ ($E_\nu > 10$ GeV)	0.01	8[d]
$\bar{\nu}_\mu/\nu_\mu$ ($E_\nu < 1$ GeV)	−0.25	2
$\bar{\nu}_\mu/\nu_\mu$ ($1 < E_\nu < 10$ GeV)	−0.36	6
$\bar{\nu}_\mu/\nu_\mu$ ($E_\nu > 10$ GeV)	1.32	6[e]
Up/down ratio	−0.50	1
Horizontal/vertical ratio	0.54	1
K/π ratio in flux	−7.54	10[f]
Neutrino path length	0.36	10
Sample-by-sample (FC multi-GeV)	−5.16	5
Sample-by-sample (PC + UPMU stopping μ)	−10.3	5
M_A in CCQE and single-π	0.77	10
CCQE cross section	5.29	1[g]
CCQE $\bar{\nu}/\nu$	8.93	1[g]
CCQE ν_μ/ν_e	5.03	1[g]
Single-π cross section	3.24	20
Single-π π^0/charged-π	−35.9	40
Single-π $\bar{\nu}/\nu$	−3.37	1[h]
DIS (low-Q^2)	−0.61	1[i]
DIS	1.85	5
Coherent-π	24.2	100
NC/CC ratio	−0.78	20
Nuclear effects in ^{16}O nucleus	−22.9	30
Nuclear effects in pion spectrum	9.30	1[j]
ν_τ contamination	−15.9	30
NC in FC μ-like (hadron simulation)	−2.17	10

[a]Uncertainty linearly decreases with $\log E_\nu$ from 25%(0.1 GeV) to 7%(1 GeV).
[b]Uncertainty is 7% up to 10 GeV, linearly increases with $\log E_\nu$ from 7%(10 GeV) to 12%(100 GeV) and then to 20%(1 TeV)
[c]Uncertainty linearly increases with $\log E_\nu$ from 5%(30 GeV) to 30%(1 TeV).
[d]Uncertainty linearly increases with $\log E_\nu$ from 8%(100 GeV) to 20%(1 TeV).
[e]Uncertainty linearly increases with $\log E_\nu$ from 6%(50 GeV) to 40%(1 TeV).
[f]Uncertainty increases linearly from 5% to 20% between 100 GeV and 1 TeV.
[g]Difference from the Nieves [32] model is set to 1.0.
[h]Difference from the Hernandez[33] model is set to 1.0.
[i]Difference from CKMT [34] parametrization is set to 1.0.
[j]Difference between NEUT [22,23] and NUANCE [35] is set to 1.0.

VII. CONCLUSIONS

We have studied nonstandard neutrino interactions in the context of atmospheric neutrinos propagating in the Earth. Two analyses were presented considering possible effects from both flavor changing neutral current and lepton universality violating interactions. Analysis of the SK-I and SK-II atmospheric neutrino data shows no evidence of NSI and provides the following constraints. For NSI in the $\nu_\mu - \nu_\tau$ sector, the two-flavor hybrid model allows contributions from NSI in the form

$$|\varepsilon_{\mu\tau}| < 1.1 \times 10^{-2} \quad \text{and} \\ -4.9 \times 10^{-2} < \varepsilon_{\tau\tau} - \varepsilon_{\mu\mu} < 4.9 \times 10^{-2}, \tag{13}$$

at the 90% C.L., where ε and ε' are replaced with $\varepsilon_{\mu\tau}$ and $\varepsilon_{\tau\tau} - \varepsilon_{\mu\mu}$, respectively. In the three-flavor hybrid model, the allowed regions are presented for different values of ε_{ee} since the atmospheric data have no ability to constrain this parameter.

ACKNOWLEDGMENTS

We gratefully acknowledge the cooperation of the Kamioka Mining and Smelting Company. The Super-Kamiokande experiment has been built and operated from funding by the Japanese Ministry of Education, Culture, Sports, Science and Technology, the United States Department of Energy, and the U.S. National Science Foundation. Some of us have been supported by funds from the Korean Research Foundation (BK21), and the Korea Science and Engineering Foundation. Some of us have been supported by the State Committee for Scientific Research in Poland (grant 1757/B/H03/2008/35).

TABLE V. Detector related systematic errors, including uncertainties from the event reduction and reconstruction from the three-flavor hybrid analysis. The systematic errors and their resulting fit differ between SK-I and SK-II. The second (fourth) column shows the fitted value of the systematic error parameter in percent for SK-I (SK-II) and the third (fifth) column shows the associated error size in percent.

Systematic Uncertainties in Event Selection	SK-I Fit (%)	SK-I σ (%)	SK-II Fit (%)	SK-II σ (%)
FC reduction	0.04	0.2	<0.01	0.19
PC reduction	−0.81	2.4	−2.62	4.8
FC/PC separation	−0.13	0.6	0.05	0.5
PC stopping/through separation (top)	11.3	15	−18.0	19
PC stopping/through separation (barrel)	−0.65	7.4	−22.4	14
PC stopping/through separation (bottom)	−7.10	11.3	−19.2	18
Non-ν_e BG in Multi-GeV single-ring e-like	2.75	14.5	−4.05	20.6
Non-ν_e BG in Multi-GeV multi-ring e-like	−12.2	39.6	5.39	12.6
Multi-GeV multi-ring e-like	−1.37	7	0.75	3.2
Non-ν BG (flasher)	0.13	0.5	−0.04	0.5
Non-ν BG (cosmic-ray muon)	−0.14	0.1	0.23	0.1
Fiducial volume	−0.18	2	0.38	2
Ring separation	5.96	10	−10.4	10
Particle identification	−0.10	1	0.17	1
Particle identification (Multi-ring)	3.16	10	4.50	10
Energy scale calibration	0.13	1.1	−1.58	2.5
Up/down asymmetry of energy calibration	0.06	0.6	−0.19	0.6
UPMU reduction	0.52	1	−0.07	1
UPMU stopping/through-going separation	−0.04	0.39	−0.00	0.41
Energy cut for UPMU stopping	−0.08	0.8	−0.04	1.1
UPMU nonshowering/showering separation	−1.68	2.8	−0.30	1.8
BG subtraction of UPMU stopping	3.43	17	−16.3	24
BG subtraction of UPMU nonshowering	−0.01	1.5	1.75	3
BG subtraction of UPMU showering	6.17	13	6.12	24
Sub-GeV 1-ring π^0 selection	−3.57	10	−5.33	10
Sub-GeV 2-ring π^0	−0.53	2	−0.28	2
Decay-e tagging	0.86	1.1	−0.06	1.1
Decay-e π^+-decay uncertainty	−6.94	10	−6.57	10
Solar activity	3.08	20	32.1	50

APPENDIX

1. Summary of systematic uncertainties

Tables II and III summarize the systematic error parameters for the best-fit point from two-flavor hybrid model analysis. Tables IV and V summarize the best-fit systematic error parameters from the fit to the three-flavor hybrid model.

[1] Y. Fukuda *et al.*, Phys. Lett. **81**, 1562 (1998).
[2] Y. Ashie *et al.*, Phys. Rev. Lett. **93**, 101801 (2004).
[3] K. Abe *et al.*, Phys. Rev. Lett. **97**, 171801 (2006).
[4] M. H. Ahn *et al.*, Phys. Rev. D **74**, 072003 (2006).
[5] P. Adamson *et al.*, Phys. Rev. Lett. **101**, 151601 (2008).
[6] P. Lipari and M. Lusignoli, Phys. Rev. D **60**, 013003 (1999).
[7] Y. Grossman and M. P. Worah, arXiv:hep-ph/9807511.
[8] E. Lisi, A. Marrone, and D. Montanino, Phys. Rev. Lett. **85**, 1166 (2000).
[9] V. Barger, J. G. Learned, S. Pakvasa, and T. J. Weiler, Phys. Rev. Lett. **82**, 2640 (1999).
[10] V. Barger *et al.*, Phys. Lett. B **462**, 109 (1999).
[11] R. Fardon, A. E. Nelson, and N. Weiner, J. Cosmol. Astropart. Phys., 10 (2004) 005.
[12] K. Abe *et al.*, Phys. Rev. D **77**, 052001 (2008).
[13] L. Wolfenstein, Phys. Rev. D **17**, 2369 (1978).
[14] B. W. Lee and R. E. Shrock, Phys. Rev. D **16**, 1444 (1977).
[15] J. Schechter and J. W. F. Valle, Phys. Rev. D **22**, 2227 (1980).
[16] L. J. Hall and M. Suzuki, Nucl. Phys. **B231**, 419 (1984).
[17] N. Fornengo *et al.*, Phys. Rev. D **65**, 013010 (2001).
[18] J. Dorenbosh *et al.*, Phys. Lett. B **180**, 303 (1986).
[19] G. P. Zeller *et al.*, Phys. Rev. Lett. **88**, 091802, (2002).
[20] Y. Ashie *et al.*, Phys. Rev. D **71**, 112005 (2005).
[21] M. Honda *et al.*, Phys. Rev. D **75**, 043006 (2007).
[22] Y. Hayato, Nucl. Phys. B, Proc. Suppl. **112**, 171 (2002).
[23] G. Mitsuka, AIP Conf. Proc. **967**, 208 (2007); AIP Conf. Proc. **981**, 262 (2008).
[24] B. Pontecorvo, Sov. Phys. JETP **26**, 984 (1968); Z. Maki, M. Nakagawa, and S. Sakata, Prog. Theor. Phys. **28**, 870 (1962).
[25] S. P. Mikheyev and A. Y. Smirnov, Sov. J. Nucl. Phys. **42**, 913 (1985).
[26] A. M. Dziewonski and D. L. Anderson, Phys. Earth Planet. Inter. **25**, 297 (1981).
[27] J. Bahcall and P. Krastev, Phys. Rev. C **56**, 2839 (1997).
[28] M. C. Gonzalez-Garcia and M. Maltoni, Phys. Rev. D **70**, 033010 (2004).
[29] M. C. Gonzalez-Garcia *et al.*, Phys. Rev. Lett. **82**, 3202 (1999).
[30] S. Davidson *et al.*, J. High Energy Phys. 03 (2003) 011.
[31] G. L. Fogli, E. Lisi, A. Marrone, D. Montanino, and A. Palazzo, Phys. Rev. D **66**, 053010 (2002).
[32] J. Nieves, J. E. Amaro, and M. Valverde, Phys. Rev. C **70**, 055503 (2004).
[33] E. Hernandez *et al.*, Phys. Rev. D **76**, 033005 (2007).
[34] A. Capella *et al.*, Phys. Lett. B **337**, 358 (1994); M. H. Reno, Phys. Rev. D **74**, 033001 (2006).
[35] D. Casper, Nucl. Phys. B, Proc. Suppl. **112**, 161 (2002).
[36] M. Blennow and T. Ohlsson, Phys. Rev. D **78**, 093002 (2008).
[37] M. Honda *et al.*, Phys. Rev. D **64**, 053001 (2001).
[38] A. Friedland and C. Lunardini, Phys. Rev. D **72**, 053009 (2005).
[39] R. Wendell *et al.*, Phys. Rev. D **81**, 092004 (2010).
[40] M. Apollonio *et al.*, Phys. Lett. B **466**, 415 (1999).